1995ApJ...448..715R

THE ASTROPHYSICAL JOURNAL, 448:715–726, 1995 August 1
© 1995. The American Astronomical Society. All rights reserved. Printed in U.S.A.

A COMPARISON OF DIFFUSE IONIZED AND NEUTRAL HYDROGEN AWAY FROM THE GALACTIC PLANE: Hα-EMITTING H I CLOUDS

R. J. REYNOLDS, S. L. TUFTE, AND D. T. KUNG[1]
Department of Physics, University of Wisconsin-Madison, 1150 University Avenue, Madison, WI 53706

AND

P. R. MCCULLOUGH[2,3] AND C. HEILES
Astronomy Department, University of California, Berkeley, CA 94720
Received 1994 September 21; accepted 1995 February 2

ABSTRACT

We compare velocity-resolved maps of the interstellar Hα emission at 1° angular resolution within a 10° × 12° region of the sky, and 3′ resolution within a 1° × 1° region, with corresponding maps of 21 cm emission. The results indicate that at least 30% of the Hα background and 10%–30% of the 21 cm emission are spatially and kinematically associated with "clouds" containing both neutral and ionized hydrogen. These Hα-emitting H I clouds, identified as prominent Hα and 21 cm emission enhancements of several degrees extent on narrow (12 km s^{-1}) velocity interval maps, have H I column densities that range from about 2×10^{19} cm^{-2} to 2×10^{20} cm^{-2} and emission measures from 2 cm^{-6} pc to 10 cm^{-6} pc. Their radial velocities suggest distances $|z|$ from the Galactic midplane that range from $|z| \lesssim 100$ pc to $|z| \approx 1$ kpc, with a $|z|$-distribution that is much thicker than that of the non–Hα-emitting H I. The high $|z|$ Hα-emitting H I clouds identified on these maps are approximately 40% ionized, have densities $n \approx 0.2$–0.3 cm^{-3}, and are associated with large filament and loop structures. The relationship between the H° and the H^+ within these clouds is not clear; however, the available data suggest that the neutral and ionized components of each cloud are spatially separated. If the clouds are photoionized, the Hα surface brightnesses imply that at $|z| \approx 1$ kpc the strength of the incident Lyman continuum flux $4\pi J \approx 2 \times 10^6$ photons cm^{-2} s^{-1}.

Subject headings: ISM: clouds — ISM: general — H II regions — radio lines: ISM

1. INTRODUCTION

Neutral atomic hydrogen and warm ($\approx 10^4$ K) ionized hydrogen are the two principal states of hydrogen in the interstellar medium at high Galactic latitudes, where the column densities of the H^+ amount to approximately one-third that of the H° (e.g., Reynolds 1991). The relationship between these two ionization states is not known but has been a subject of considerable speculation. It has been proposed, for example, (1) that the H^+ is confined to the outer skin of neutral hydrogen clouds embedded within a pervasive hot medium (McKee & Ostriker 1977), (2) that the H^+ is the fully ionized portion of a pervasive warm neutral medium (Miller & Cox 1993), (3) that the diffuse H^+ is associated primarily with the walls of superbubbles, "chimneys," and "worms" (Norman 1991; Koo, Heiles, & Reach 1992), and (4) that the H^+ is mixed with the neutral hydrogen, forming partially ionized clouds (Spitzer & Fitzpatrick 1993; Sciama 1990).

As a first step in exploring the relationship between the H^+ and the H°, we compare below the radial velocity and angular distributions of the diffuse Hα and 21 cm emissions over a small portion of the sky at moderate Galactic latitude. The data are presented in the form of narrow radial velocity interval maps at both 1° and 3′ angular resolution. Like other studies of clouds that involve morphological comparisons of different interstellar medium tracers, this paper is a mixture of quantitative analysis with some qualitative interpretation. The result reveals that there is much to learn about the nature of interstellar clouds from comparisons of Hα and 21 cm maps.

2. 1° RESOLUTION MAPS

The Hα data are from the Fabry-Perot observations of Reynolds (1980), which consisted of 121 Hα scans with a 0.°8 diameter beam on a grid of directions spaced at 6^m intervals in R.A. from 1^h58^m to 2^h58^m and 1° intervals in declination from +32.°9 to +42.°9 (epoch 1950). The center of this map has Galactic coordinates $l = 144°$, $b = -21°$. The radial velocity interval sampled was from -120 km s^{-1} to $+50$ km s^{-1} (LSR) at a resolution of 12 km s^{-1}. The limiting sensitivity (3 σ) to an Hα emission component with a line width of 24 km s^{-1} (FWHM) is 5×10^{-8} ergs cm^{-2} s^{-1} sr^{-1} (0.2 R), which corresponds to an emission measure of 0.5 cm^{-6} pc. These data, which were originally obtained to explore the kinematics and angular distribution of the diffuse H^+, provide a suitable data set with which to compare the 21 cm emission.

The 21 cm data were obtained in 1991–1992 with the Hat Creek radio telescope (now destroyed) over a somewhat larger region of the sky and higher angular resolution than the Hα data. The observations consisted of 945 scans with a 0.°6 diameter beam on a $4^m \times 0.°6$ grid within a hexagonal region located between R.A. = 1^h30^m and 3^h30^m and decl. = +30° and +50°. The radial velocity interval sampled was from -152 km s^{-1} to $+111$ km s^{-1} at a resolution of 2.1 km s^{-1}. The limiting sensitivity to a 21 cm emission component (24 km s^{-1} FWHM) is ~ 3 K km s^{-1}, which is due primarily to baseline and sidelobe uncertainties and corresponds to a column density $N_{HI} \approx 5 \times 10^{18}$ cm^{-2}. These 21 cm observations have

[1] Current address: Department of Mathematics, University of Wisconsin-Madison, 480 Lincoln Drive, Madison, WI 53706.
[2] Hubble Fellow.
[3] Current address: Astronomy Department, University of Illinois, Urbana, IL 61801.

© American Astronomical Society • Provided by the NASA Astrophysics Data System

1995ApJ...448..715R

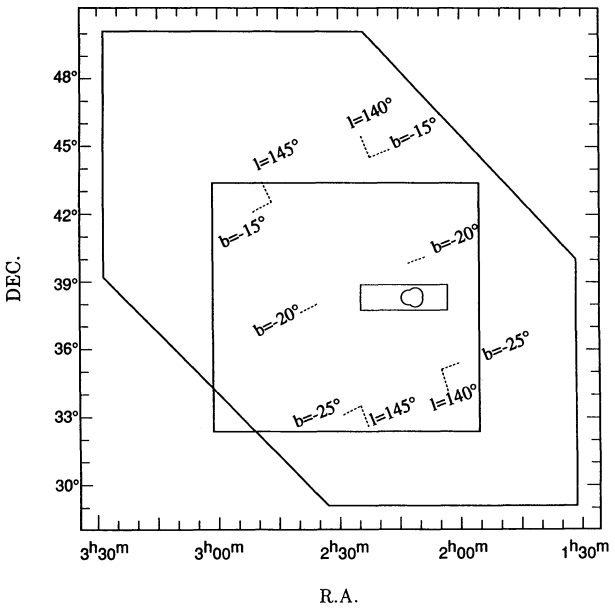

FIG. 1.—Borders of the Hat Creek H I map (*hexagon*), 1° angular resolution Hα map (*square*), Arecibo H I map (*rectangle*), and 3′ angular resolution Hα map (*oval*).

~4 times the sensitivity of the earlier "all-sky" Hat Creek survey, which made possible the detection of 21 cm features not seen on the earlier survey. The borders of the Hα and 21 cm maps are shown in Figure 1. Note that there is no 21 cm data for the southeast corner (three pixels) of the Hα map.

In Figure 2 (Plates 26–27) the Hα data and the 21 cm data within the region mapped in Hα are displayed as a series of radial velocity interval maps generated by integrating the interstellar emission-line profiles within seven contiguous 12 km s^{-1} radial velocity intervals centered from −70 km s^{-1} to +2 km s^{-1} (LSR). An eighth map shows the velocity-integrated Hα and 21 cm intensity distributions. A 12 km s^{-1} interval was chosen for display because it is the resolution of the Hα spectrometer and is approximately one-half the width of a typical interstellar Hα component. Thus the kinematics of the H^+ are fully sampled. This interval is also approximately the velocity width of the 21 cm features found on the maps (see Table 1). Velocity intervals more negative than −70 km s^{-1} and more positive than +2 km s^{-1} reveal no additional emission structures. To facilitate comparisons of features between the two data sets, the maps are displayed in 21 cm–Hα pairs at the same velocity interval, and the 21 cm maps have been cropped to the size of the Hα map. Also, for Figure 2 the somewhat higher angular resolution 21 cm maps have been smoothed to the same angular resolution as the Hα. The display transfer function is logarithmic, and the gain and the offset were chosen individually for each image so that the emission enhancements can be clearly seen. The brightest areas of each map are red.

3. COMPARISONS OF Hα AND 21 cm EMISSION AT 1° ANGULAR RESOLUTION

3.1. *Total Intensities*

How representative this mapped area is of the interstellar medium cannot be answered with certainty until a more comprehensive Hα survey is carried out. However, the intensities and intensity fluctuations in this region do appear to be "typical" for this latitude. Figure 3 shows the distribution of total interstellar Hα intensities and 21 cm column densities (corrected for csc $|b|$) for the 118 pixels having both Hα and 21 cm data. The Hα intensity is in rayleighs (R), where 1 R = $10^6/4\pi$ photons cm^{-2} s^{-1} sr^{-1}. The mean value for $I_\alpha \sin|b|$ is 1.2 R with a standard deviation of 0.5 R, which is not affected significantly by the measurement uncertainty. These values are nearly identical to those derived from a "random, all-sky" sample of the interstellar Hα background at $|b| > 15°$ and decl. > −10° (see Reynolds 1992, 1993). For the 21 cm data the mean value of $N_{\rm H\,I} \sin|b|$ is 2.3×10^{20} cm^{-2} with a standard deviation of 4.3×10^{19} cm^{-2}. This mean is close to the all-sky mean of 2.9×10^{20} cm^{-2}, while the standard deviation is significantly smaller than the all-sky value of 1.4×10^{20} cm^{-2} (Dickey & Lockman 1990). However, Dickey & Lockman point out that the large scatter in the all-sky data is due in part to several large, isolated H I concentrations that lie far from the plane.

A pixel-by-pixel comparison between the total Hα and 21 cm emission in this region suggests that there is no strong relationship between the neutral and ionized gas. This is illustrated in Figure 4, which shows that the weak correlation between I_α and $N_{\rm H\,I}$ (Fig. 4*a*) almost disappears when $I_\alpha \sin|b|$ is plotted against $N_{\rm H\,I} \sin|b|$ (Fig. 4*b*), implying that the apparent correlation is due primarily to the fact that both the Hα and the 21 cm intensities follow the csc $|b|$ law. Further, the shapes of the Hα and 21 cm distributions in Figure 3 are quite different. The Hα distribution is sharply peaked near the mean with a high-intensity tail extending more than a factor of 2 from the mean. The $N_{\rm H\,I}$ distribution, on the other hand, is relatively flat with

TABLE 1

Hα AND 21 cm EMISSION ENHANCEMENTS

	Hα			21 cm			
FEATURE	EM (cm^{-6} pc)	$V_{\rm LSR}$ (km s^{-1})	FWHM (km s^{-1})	$N_{\rm H\,I}$ (10^{19} cm^{-2})	$V_{\rm LSR}$ (km s^{-1})	FWHM (km s^{-1})	EM/$N_{\rm H\,I}$ (10^{-19} cm^{-4} pc)
A.....	11 ± 1	+1 ± 2	21 ± 2	21 ± 3	0 ± 2	8.9 ± 1.0	0.52 ± 0.09
B.....	2.1 ± 0.6	−22 ± 3	26 ± 2	...	...	...	...
C.....	2.3 ± 0.3	−48 ± 2	37 ± 2	7.5 ± 2	−47 ± 2	25 ± 3	0.30 ± 0.09
D	4.4 ± 1.0	−46 ± 3	37 ± 3	9.8 ± 3.0	−53 ± 3	13 ± 2	0.45 ± 0.17
E.....	1.6 ± 0.4	−67 ± 3	25 ± 2	1.4 ± 0.3[a]	−63 ± 4	23 ± 4	1.1 ± 0.4
F.....	0.6 ± 0.3	−60 ± 5	23 ± 6	4.1 ± 0.2	−57 ± 2	18 ± 2	0.15 ± 0.08
G	<0.3[b]	...	...	21 ± 2	−1 ± 1	6.9 ± 0.3	<0.014

[a] The high angular resolution Arecibo data indicate column densities approximately twice this value (see § 4).
[b] For an Hα line width of 25 km s^{-1} (FWHM).

© American Astronomical Society • Provided by the NASA Astrophysics Data System

1995ApJ...448..715R

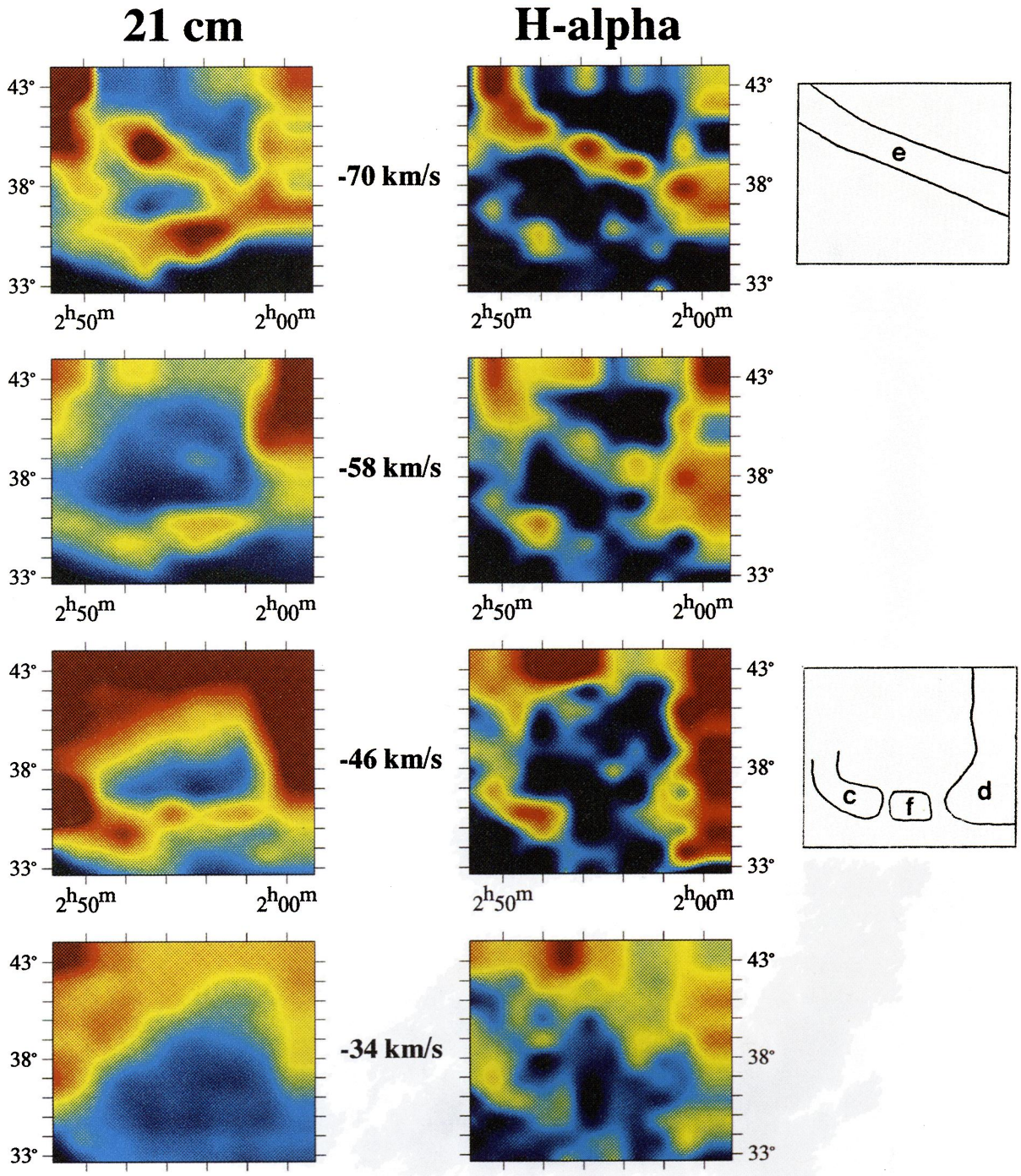

FIG. 2a

FIG. 2.—Pairs of 21 cm and Hα velocity interval maps covering R.A. = 1^h58^m–2^h58^m, decl. = +32°.9–+42°.9. Scales on each frame have been adjusted to show the associated 21 cm and Hα emission features. Red denotes areas of maximum intensity. The center of the 12 km s^{-1} radial velocity interval for each pair of frames is also indicated; frames labeled "total" are for the velocity interval −100 km s^{-1} to +20 km s^{-1} (LSR). Schematic outlines to the right of some of the Hα frames identify the 21 cm and Hα emission features discussed in the text.

REYNOLDS et al. (see 448, 716)

© American Astronomical Society • Provided by the NASA Astrophysics Data System

1995ApJ...448..715R

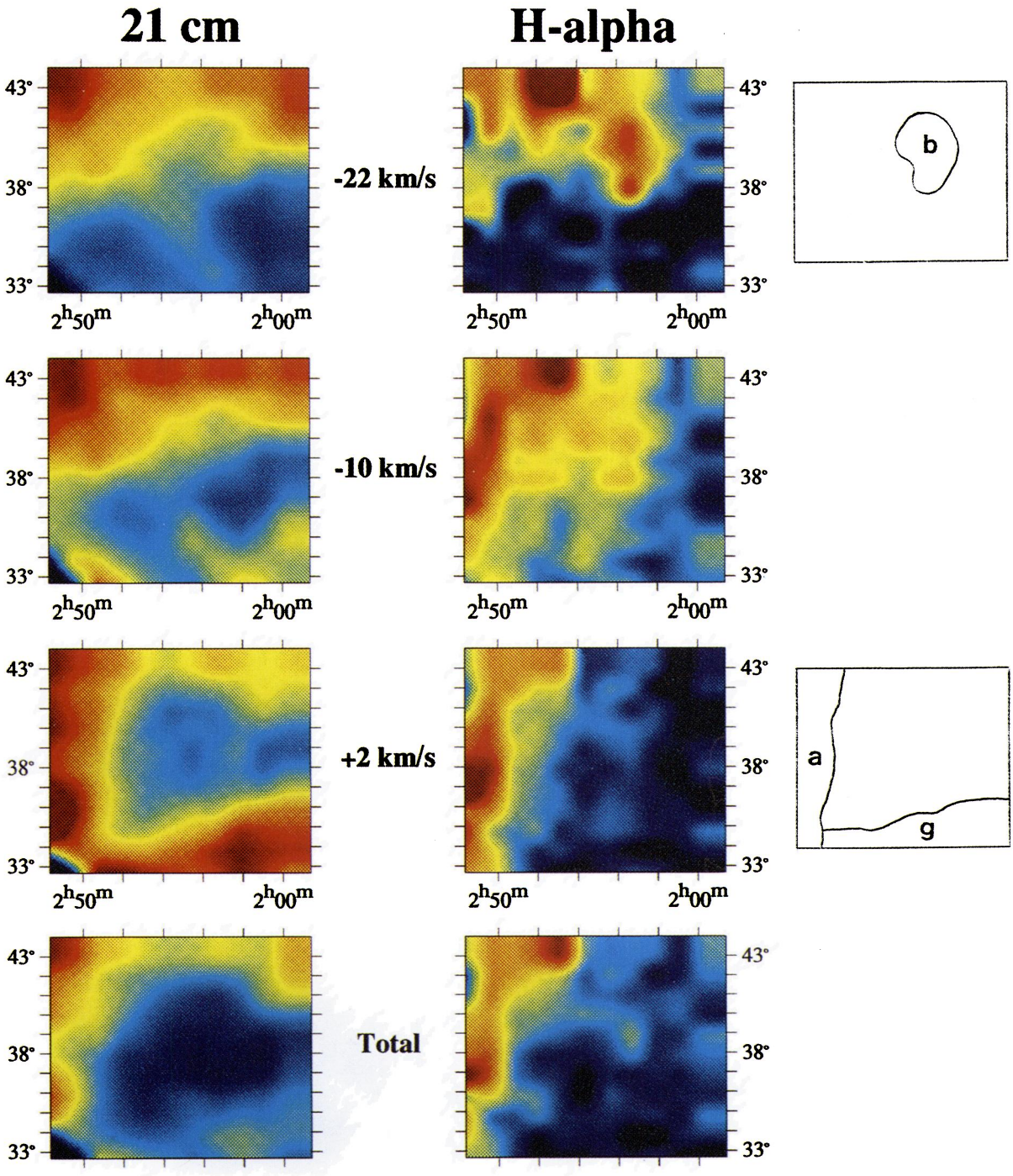

FIG. 2*b*

REYNOLDS et al. (see 448, 716)

© American Astronomical Society • Provided by the NASA Astrophysics Data System

1995ApJ...448..715R

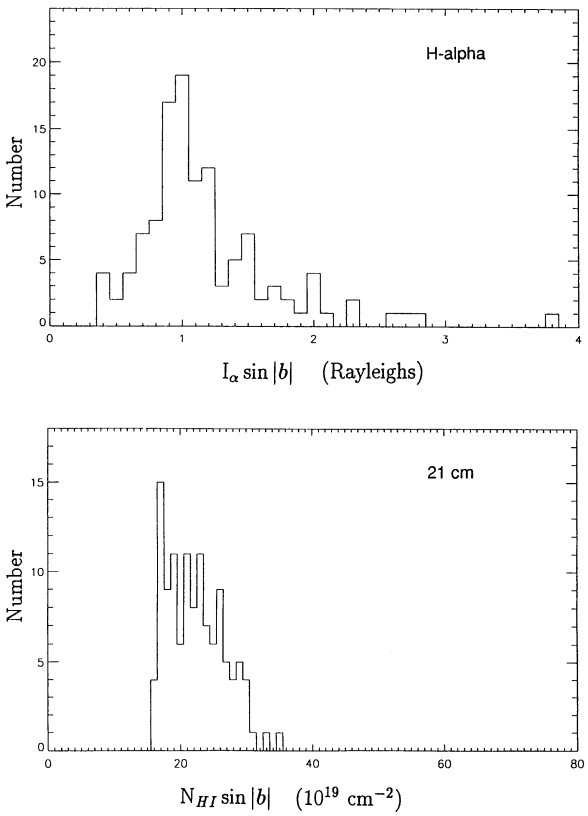

FIG. 3.—Distributions of $I_\alpha \sin|b|$ and $N_{\rm H\,I} \sin|b|$ in the total intensity maps of Fig. 2.

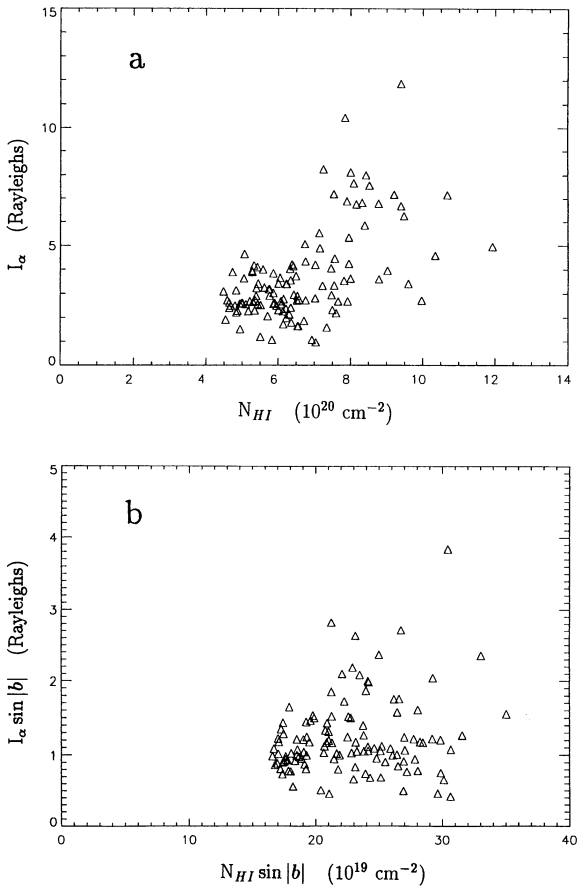

FIG. 4.—I_α vs. $N_{\rm H\,I}$ in the total intensity maps for each of the 118 pixels for which there is both Hα and 21 cm data: (*a*) actual intensities; (*b*) intensities corrected for the cosecant $|b|$ effect.

no extended wings. This is a reflection of the fact that there is much more contrast in the Hα map than the 21 cm.

The difference in contrast between the Hα and 21 cm maps is illustrated in Figure 5, where the absolute Hα and 21 cm intensities are plotted versus declination for the R.A. interval of 2^h37^m–2^h49^m (1950). In the top total intensity plot, the ratio of maximum to minimum intensity is 3.7 in the Hα and only 1.5 in the $N_{\rm H\,I}$. Moreover, a significant Hα intensity enhancement centered at decl. $\simeq +36°$ appears to have little or no counterpart in the $N_{\rm H\,I}$. Higher contrast in the Hα compared to H I also holds for the narrow-velocity interval maps, although the effect diminishes at higher absolute velocities. This can be seen, for example, in the lower plot of Figure 5, where the same R.A. cut is shown, but only for the -52 km s^{-1} to -40 km s^{-1} velocity interval. In this narrow velocity interval, there appears to be much more correspondence between the Hα and H I. The Hα enhancement at $+36°$ is more prominent, and a corresponding enhancement is now apparent in the H I. This example plus an examination of the velocity-resolved data over the entire mapped region suggest that the velocity-integrated $N_{\rm H\,I}$ map is dominated by 21 cm emission near the LSR that has little relationship to the Hα and dilutes the weaker features at higher $|v|$, some of which in fact do have a correspondence with Hα features. The velocity interval maps are thus a more sensitive probe of correlations between the neutral and ionized gas.

3.2. *Velocity Interval Maps*

The velocity interval maps in Figure 2 reveal that both the neutral and ionized gas in this region have complex spatial and kinematic structure, with regions of enhanced emission superposed on a more diffuse background. One striking aspect of the maps is that all of the large ($>2°$), prominent regions of Hα enhancement appear to have an associated feature at 21 cm. Thus, even though the correlation on the total intensity data is weak, there is nevertheless a clear spatial and kinematic relationship between *some* of the neutral and ionized hydrogen. The brightest Hα emission feature, which occupies the eastern edge of the map on the $+2$ km s^{-1} frame, coincides with part of an H I "cloud" at the same velocity. Similarly, the Hα enhancements centered near 2^h45^m $+36°$ and 2^h00^m $+40°$ in the -46 km s^{-1} frame and the long filament stretching from 2^h54^m $+42°$ to 2^h00^m $+37°$ in the -70 km s^{-1} frame are clearly associated with corresponding enhancements at 21 cm. Not all the correlations are positive, however. The 3° diameter Hα emission enhancement centered at 2^h15^m $+40°$ in the -22 km s^{-1} frame seems to coincide with a deficit in the emission on the corresponding 21 cm frame. Also, the small 21 cm "cloud" at 2^h20^m–2^h30^m $+36°$ in the -46 km s^{-1} and -58 km s^{-1} frames is located in a gap between two larger pincher-shaped regions of Hα enhancement in the -46 km s^{-1} frame. Finally, there is one prominent region of 21 cm enhancement, along the southern border of the $+2$ km s^{-1} frame, which has no corresponding Hα enhancement or deficit.

To facilitate a more quantitative comparison of the regions of Hα and 21 cm enhancement, eight areas of the map were

© American Astronomical Society • Provided by the NASA Astrophysics Data System

1995ApJ...448..715R

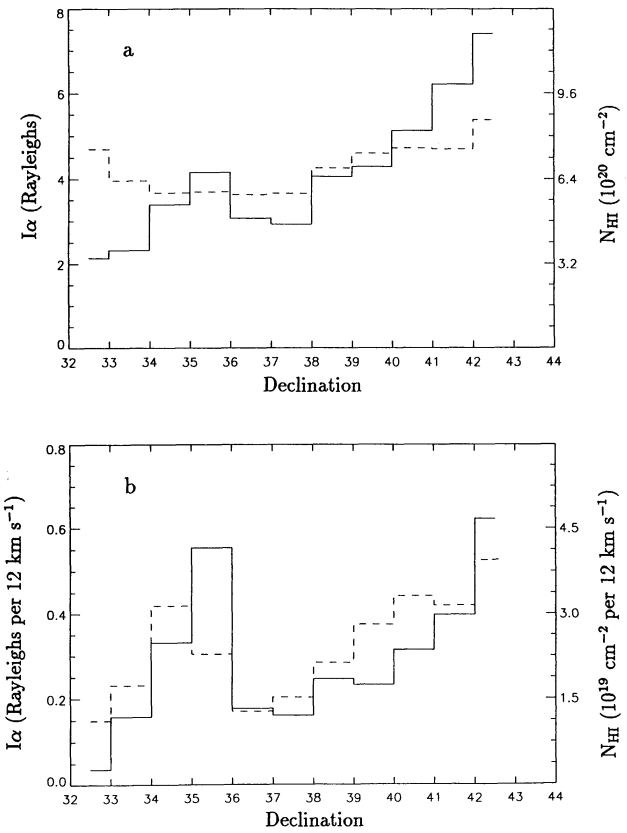

FIG. 5.—Average I_α (*solid line*) and N_{HI} (*dashed line*) vs. declination within the right ascension interval 2^h37^m–2^h49^m, showing the difference in contrast between the 21 cm and Hα maps: (*a*) from the total intensity map; (*b*) from the -46 km s^{-1} velocity interval map.

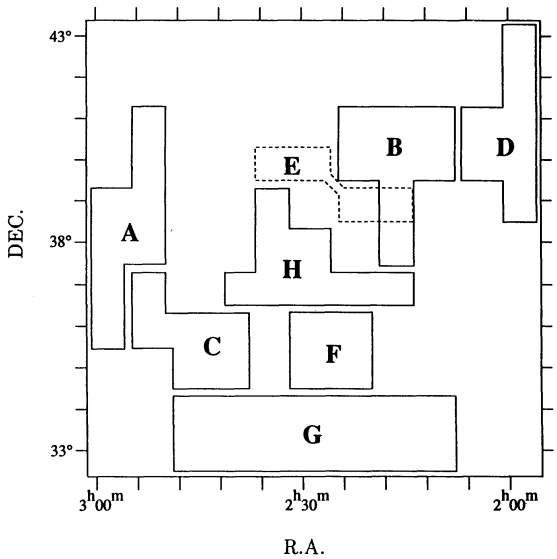

FIG. 6.—Areas analyzed on the 21 cm and Hα velocity interval maps. Areas A–G are selected regions within the emission features outlined as a–g in Fig. 2. A and G: emission features on the +2 km s^{-1} frames. B: Hα emission feature on the -22 km s^{-1} frame. C, D, and F: features on the -46 km s^{-1} frames. E: emission feature on the -70 km s^{-1} frames. H: region with no emission enhancement on any of the 21 cm or the Hα frames.

defined, and the spectra within each area were averaged. This allowed us to derive mean values for the intensity, radial velocity, and line width associated with each prominent emission feature. The areas labeled A through E on Figure 6 sample "representative" portions of the five Hα emission enhancements mentioned above and originally identified in Reynolds (1980). Area F is the gap between the Hα regions sampled by areas C and D (see the -46 km s^{-1} Hα frame in Fig. 2), while area G is the relatively bright 21 cm enhancement at +2 km s^{-1} with no corresponding Hα feature. The full extent of the emission features sampled by the areas A through G appear to have a total covering factor on the map near unity. Only one area of the map, area H, appears to be free of emission associated with any of the regions of enhanced Hα and 21 cm emission defined above. Area H thus samples the "background" between the prominent enhancements.

The properties of the emission features A through G were determined by subtracting the mean spectrum of area H from the mean spectrum of each of the other areas. Examples of the resulting spectra for area C are shown in Figure, 7, where the intensity enhancements associated with area C are clearly seen as spectrally resolved emission lines centered near -50 km s^{-1} in both the Hα and 21 cm difference spectra. For this case there is incomplete subtraction of emission near the LSR and an oversubtraction near -20 km s^{-1}. The uncertainty in the derived parameters for the region C emission enhancement is due primarily to these baseline uncertainties. The results for all of the enhancements are summarized in Table 1.

The emission measures were derived from the Hα intensity with no correction for interstellar extinction, so that EM $\simeq 2.25\, I_\alpha\, (T/8000)^{0.9}$ cm^{-6} pc, where I_α is in rayleighs (R) and T is the electron temperature in K. A temperature of 8000 K has been adopted because the line widths of the Hα components are consistent with values measured for the warm ionized medium in other directions (Reynolds 1985), where $T \approx 8000$ K and thermal and nonthermal broadening are about equally important. Errors in the value of EM due to interstellar extinction are relatively small; the total H I column densities are typically about 6×10^{20} cm^{-2} (Fig. 4*a*), implying $E(B-V) \simeq 0.1$ and optical depths at Hα of $\tau_\alpha \approx 0.2$ (Bohlin, Savage, & Drake 1978; Mathis 1983). This will result in an underestimate by a factor of 0.8 in the value of EM for the most distant Hα regions, that is, those behind nearly all the H I.

3.3. *The* Hα–H I *Clouds*

There are four features (A, C, D, and E) that are characterized by prominent emission enhancements on both the Hα and 21 cm velocity interval maps. The H° and H$^+$ in these regions are clearly associated spatially and kinematically. The emission measures and H I column densities vary by an order of magnitude, but they have EM/N_{HI} ratios that are consistent to within the measurement uncertainties with a value of $\approx$0.4–0.5 in units of cm^{-6} pc per 10^{19} cm^{-2} (see Table 1). The size of the EM/N_{HI} ratio implies that these are truly ionized clouds and not faint reflection nebulosity. Jura (1979) has calculated that the dust within high-latitude H I clouds could scatter Hα from bright H II regions in the Galactic plane, producing an Hα surface brightness of about 0.01 R (equivalent to EM = 0.023 cm^{-6} pc) per 10^{19} cm^{-2} of H I. However, this is a factor of 20 below that observed for these clouds. Jura also pointed out that the peculiar velocity of the cloud will result in a difference between the radial velocity of the reflected Hα and the 21 cm emission that is approximately equal to the peculiar velocity of the cloud. No such radial velocity difference is present in these

© American Astronomical Society • Provided by the NASA Astrophysics Data System

1995ApJ...448..715R

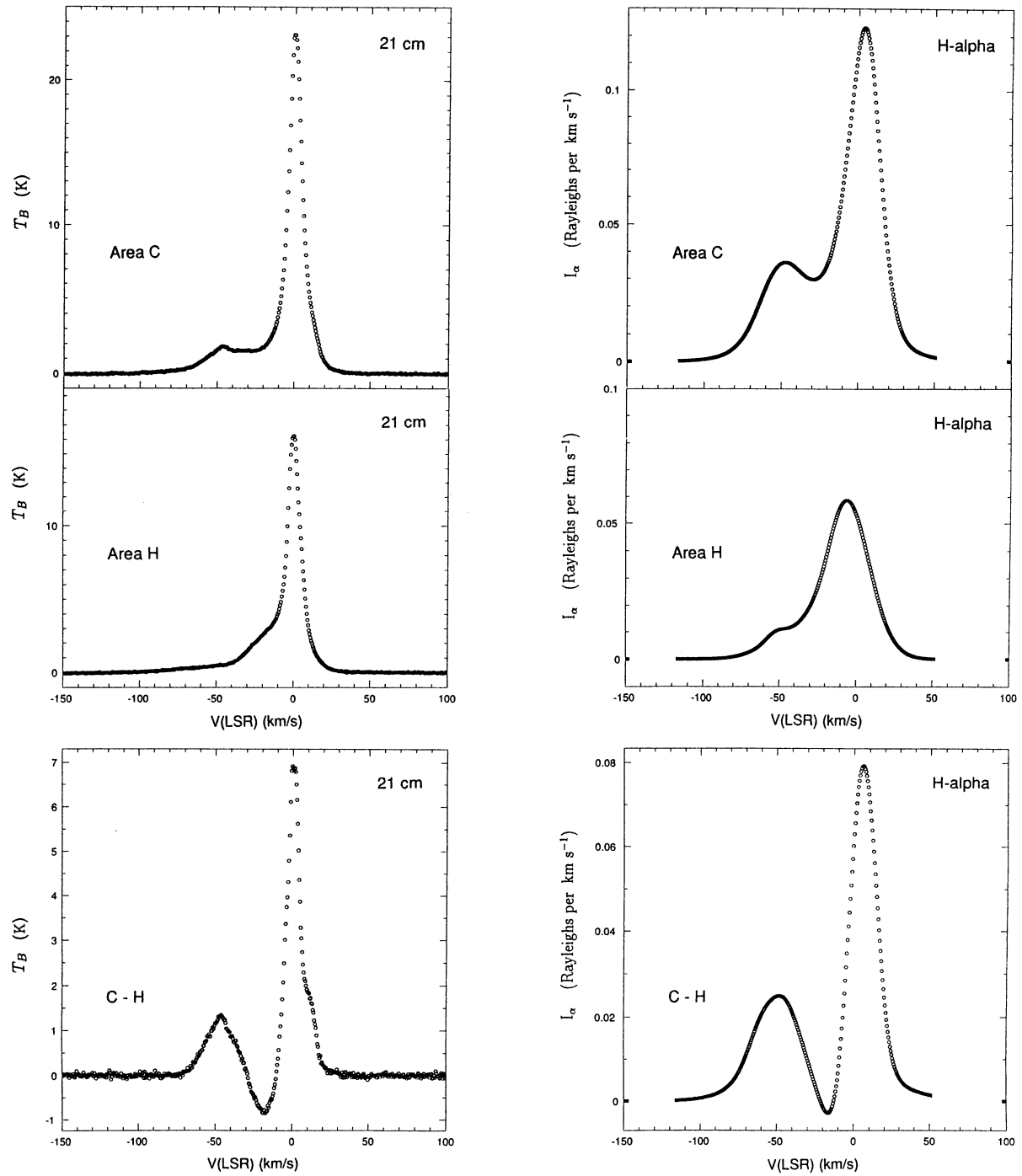

FIG. 7.—The 21 cm and Hα spectra of the emission enhancement in area C and of the more diffuse "background" in area H. The difference spectra C − H show the emission component at −50 km s^{-1} associated with the 21 cm and Hα enhancements in area C.

data. Finally, for feature E (Ogden & Reynolds 1985) and for feature A (Reynolds 1985) it has been shown that the [S II]/Hα and [O III]/Hα line intensity ratios are significantly different from those observed in bright H II regions, ruling out reflected light as the source of the optical lines.

In the remainder of this paper we will call these regions "Hα–H I clouds." The Hα–H I clouds are distinct from the Hα enhancement B, which has no associated H I, and the 21 cm enhancement G, which has no associated Hα. It is, of course, not clear from this small sample whether these Hα–H I clouds are truly a distinct class or simply represent the middle region of a continuous spectrum of $EM/N_{H\,I}$ values for interstellar clouds. For example, higher signal-to-noise techniques toward some intermediate- and high-velocity H I clouds have provided detections of very weak associated Hα emission with corresponding $EM/N_{H\,I} \approx 0.02$–0.06 (Kutyrev & Reynolds 1989; Münch & Pitz 1990; Songaila, Bryant, & Cowie 1989). Thus, it is possible that all interstellar H I emits Hα at some level (e.g.,

© American Astronomical Society • Provided by the NASA Astrophysics Data System

1995ApJ...448..715R

due to ionization by cosmic rays; see § 6). However, as is shown below, the relatively bright Hα–H I clouds identified in Figure 2 and Table 1 are associated with only a relatively small fraction of the H I and have a thicker distribution about the Galactic midplane than the H I that has little or no detectable Hα.

3.4. *Distances and Densities*

The properties of the emission features listed in Table 1 are obtained directly from the observations and represent the basic results of the 1° resolution observations. Additional information about the nature of these enhancements relies on a determination of their distances. Fortunately, the Galactic longitude interval of $l = 136°$–$152°$ covered by the map provides for good kinematic separation of the emitting regions along the line of sight due to the differential rotation of the Galactic disk. If we assume that the radial velocities of the emission features are related primarily to this large-scale differential motion, then the distances, sizes, densities, and $|z|$-heights of the regions can be estimated. This assumption seems justified because all of the emission profiles within the mapped region are asymmetric toward negative velocities, with no extended red wings, which is just what is predicted at this longitude by differential rotation. Furthermore, within this longitude interval at low Galactic latitudes the Perseus spiral arm, located at a distance $d \simeq 2.5$–3.0 kpc, appears as a resolved emission enhancement at about -40 to -50 km s^{-1} (LSR) on 21 cm and Hα spectra (e.g., Weaver & Williams 1973, 1974; Reynolds 1983). A similar but weaker velocity component is present in these higher latitude data (e.g., Fig. 7), strongly suggesting that the high negative velocity emission in these maps is associated with high $|z|$ extensions of this more distant arm.

A study by Joncas, Roger, & Dewdney (1989) indicates an average radial velocity gradient of approximately -20 km s^{-1} kpc^{-1} out to a distance of 4–5 kpc, which includes the effects of both circular and noncircular motions toward the Perseus spiral arm at $l = 127°$. If the velocity gradient is proportional to sin $2l$, then within the mapped region at latitude b, the distance d to a cloud with radial velocity v can be estimated from the relation

$$d \approx 50 \frac{|v|}{\cos^2 b} \text{ pc}, \quad (1)$$

where v is in km s^{-1}. In the absence of high peculiar velocities, that is, $|v_p| > 12$ km s^{-1} with respect to the LSR, the velocity interval maps could then be considered a series of contiguous 700 pc thick slabs of the interstellar medium extending from within 500 pc of the Sun at $|z| < 200$ pc out to a distance of 3 kpc or more with $|z| \gtrsim 1$ kpc. Equation (1) is certainly an oversimplification, since large-scale deviations from circular motion near the Perseus arm contribute to the observed velocity gradient (Miller 1968). In particular, the gradient may be significantly shallower out to about 2 kpc, resulting in a greater distance for feature B than that given by equation (1). In fact, if feature B is an H II region associated with HD 14633 (Reynolds 1980), then its distance must be that of the star, 2100 pc (Cruz-Gonzales et al. 1974), rather than the 1200 pc derived here from equation (1). However, since the radial velocity gradient used above is tied to objects in the Perseus arm (Joncas et al. 1989), equation (1) should provide relatively accurate kinematic distances for $d \gtrsim 2.5$ kpc.

Table 2 lists the resulting values for d and $|z|$ for each of the emission features. The value of v used in equation (1) is the average from the Hα and 21 cm data (Table 1). Also listed are the approximate angular size θ_{min} of the narrower dimension of the region and the corresponding linear size $L \equiv \theta_{min} d$. If cylindrical geometry is assumed, then the column density of the H^+ is given by $N_{H\,II} \simeq (EM\theta_{min} d)^{1/2}$, and the ionized and neutral volume densities are given by $n_{H\,II} \simeq (EM/\theta_{min} d)^{1/2}$ and $n_{H\,I} \simeq N_{H\,I}/\theta_{min} d$, respectively. These quantities and the ionized to neutral hydrogen column density ratio are listed in the last four columns of Table 2 for each feature. The kinematic distances to features A and G are less than 100 pc. However, this would place them inside the Local Bubble, which is known to be devoid of clouds with $N_{H\,I} \sim 10^{20}$ cm^{-2} (e.g., Cox & Reynolds 1987). Therefore, we have adopted a distance of 300 pc, which is the approximate distance to the nearest complex of gas clouds in this direction, the Per OB 2 association (Sancisi 1974). The angular sizes of D and G, whose full extent is not included in Figure 2, were obtained from the larger 21 cm data set (see Fig. 1), and θ_{min} of feature E is from Ogden and Reynolds (1985).

Table 2 indicates that the Hα–H I clouds (A, C, D, and E) all have ionized hydrogen column densities $N_{H\,II} \simeq 2$–6×10^{19} cm^{-2}, which for the high $|z|$ clouds (C, D, and E) is ~50%–80% of $N_{H\,I}$. All the high $|z|$ clouds have neutral gas volume densities $n_{H\,I} \simeq 0.3$ cm^{-3}, approximately 1 order of magnitude lower than $n_{H\,I}$ of the low $|z|$ clouds, A and G.

It must be emphasized that the results listed in Table 2 rest upon the assumption that the observed emission features are actual density enhancements (i.e., clouds) locally at rest within a thick, corotating Galactic disk. The radial velocity distributions of the Hα and 21 cm emissions at lower latitudes support this picture; however, large-scale disturbances in the velocity field along the line of sight could mimic localized density enhancements (e.g., Burton 1971). Also, most of the enhance-

TABLE 2

DISTANCES, SIZES, AND DENSITIES

Feature	d (pc)	$\|z\|$ (pc)	θ_{min}	L_{min} (pc)	$N_{H\,II}$ (10^{19} cm^{-2})	$n_{H\,II}$ (cm^{-3})	$n_{H\,I}$ (cm^{-3})	$N_{H\,II}/N_{H\,I}$
A	300[a]	90	2°	10	3.3	1.0	6.4	0.16
B.....	1200	420	3	65	3.6	0.18	...	...
C	2700	1000	1.5	72	3.9	0.18	0.34	0.52
D	2800	970	2	98	6.4	0.21	0.33	0.65
E.....	3700	1200	0.5[b]	32[b]	2.2[b]	0.23[b]	0.28[b]	0.79
F.....	3500	1400	1.5	91	2.3	0.08	0.15	0.57
G	300[a]	130	4	21	<0.8	<0.12	3.2	<0.04

[a] Assumed, not kinematic, distance (see text).

[b] These parameters use $N_{H\,I} \simeq 2.8 \times 10^{19}$ cm^{-2} and θ_{min} derived from the high angular resolution observations.

© American Astronomical Society • Provided by the NASA Astrophysics Data System

1995ApJ...448..715R

ments appear to be associated with loops, shells, and filaments (see § 5 below) and therefore could have significant peculiar velocities with respect to the ambient medium. Unambiguous information about the distances and kinematics of such clouds must await additional observations.

3.5. *The Background Emission*

Most of the Hα and 21 cm emission within the mapped region is not associated with the discrete regions (A–G) identified on the velocity interval maps. For the Hα this can be seen, for example, from the fact that the average EM sin $|b|$ toward areas G and H, where there is no identifiable Hα emission enhancement, is 1.8 cm^{-6} pc and 2.1 cm^{-6} pc (0.80 R and 0.93 R), respectively, which is 65%–75% of the average EM sin $|b|$ within the mapped region (Fig. 3). Thus the identified features account for only about 30% of the Hα emission. The fraction of the emission in this "background" is even higher at 21 cm. In area H, the only region free of prominent 21 cm enhancements on the velocity interval maps, $N_{\rm H\,I}$ sin $|b| \simeq 1.8 \times 10^{20}$ cm^{-2}, which is about 80% of the map average. If we take into account the fact that enhancements B and G are not Hα–H I clouds, we conclude that the identified Hα–H I clouds account for approximately 27% of the Hα and 10% of the 21 cm emission within the mapped region.

The nature of the emitting gas that accounts for this relatively smooth background cannot be readily investigated on maps of such limited angular size. It is possible, for example, that the background Hα is due to larger and/or fainter regions (Hα–H I clouds?) that simply cannot be identified as discrete enhancements on this map. However, while unidentified Hα–H I clouds could account for most of the background Hα, they could not account for most of the background H I. Since EM/$N_{\rm H\,I} \simeq 0.4$ cm^{-6} pc per 10^{19} cm^{-2} for the Hα–H I clouds, the background EM of 2.1 csc $|b|$ cm^{-6} pc (area H) could account for at most an $N_{\rm H\,I}$ of 5.3×10^{19} csc $|b|$ cm^{-2}, only about 30% of the estimated "background" H I. Therefore, at least 70% of the background 21 cm must be neutral hydrogen regions with little or no associated Hα emission. This is the low-velocity H I that dominates the total intensity data discussed in § 3.1.

The Hα and 21 cm spectra in area H (Fig. 7) show that both the neutral and ionized hydrogen profiles for the background are asymmetric with extended tails toward high negative velocities (large distances from the midplane). The H I also appears to be more concentrated to low velocities (the Galactic midplane) than the Hα. This is shown more quantitatively in Figure 8, in which the ratio EM/$N_{\rm H\,I}$ is plotted as a function of radial velocity (and $|z|$). For this plot, the average 21 cm line profile near area H from the Bell Laboratory survey (Stark et al. 1992) was used instead of the Hat Creek data to avoid biases at high velocities (high $|z|$) due to sidelobe contamination. A comparison of the Bell Laboratory and Hat Creek line profiles over the mapped region indicates that such contamination is significant in the Hat Creek data at $v < -50$ km s^{-1}, with a maximum effect of $\sim 50\%$ near -80 km s^{-1}. Also, before dividing the Hα by the 21 cm profile, the latter was convolved with a unit area Gaussian of FWHM 25 km s^{-1} so that the narrower component line widths of the 21 cm emission, particularly the emission near the LSR, would not significantly affect this comparison with the Hα. The result (*solid line* in Fig. 8) shows that EM/$N_{\rm H\,I}$ increases with $|v|$ from EM/$N_{\rm H\,I} \simeq 0.10$ cm^{-6} pc per 10^{19} cm^{-2} near the LSR to 0.27 cm^{-6} pc per 10^{19} cm^{-2} at $v = -50$ km s^{-1}. The corresponding height $|z|$ from the midplane is indicated along the top of Figure 8. Low EM/$N_{\rm H\,I}$ gas is clearly concentrated near the midplane, while higher values of EM/$N_{\rm H\,I}$, approaching those observed in the Hα–H I clouds, are found at $|z| \approx 1$ kpc. The decrease in EM/$N_{\rm H\,I}$ at velocities more negative than -60 km s^{-1} is not significant; the Hα and 21 cm signals are very weak in this range and thus sensitive to the small uncertainties in the baseline levels. A comparison of the background EM/$N_{\rm H\,I}$ ratio variation with that for the entire mapped region (*dotted line*) suggests that the distribution of neutral and ionized gas in the "background" is not much different from sightlines that include the identified enhancements.

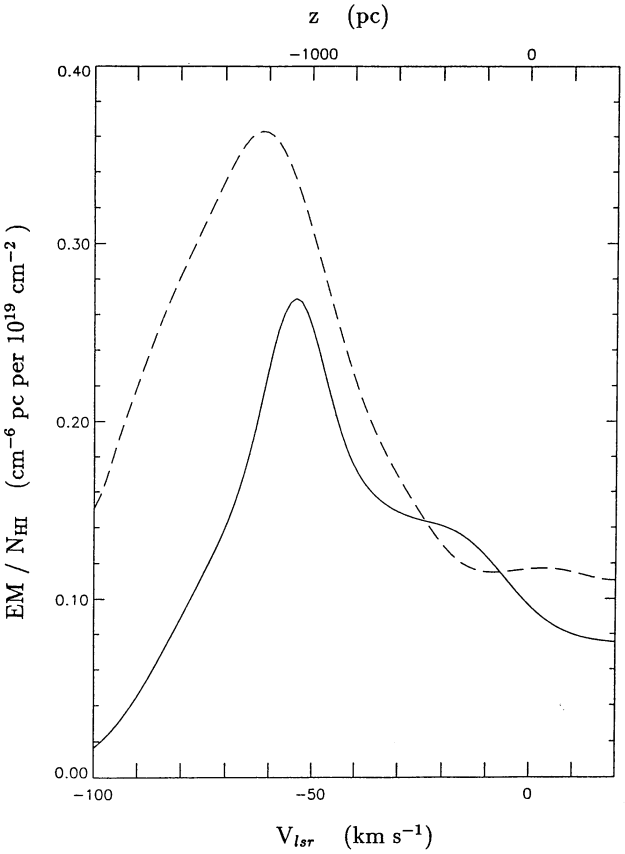

FIG. 8.—EM/$N_{\rm H\,I}$ ratio vs. radial velocity and height $|z|$ from the Galactic midplane. *Solid line* denotes only area H; *dashed line* denotes average for entire map. The 21 cm emission profile was broadened by 25 km s^{-1} to more closely match the Hα profile (see text).

4. Hα AND 21 CENTIMETER AT HIGH ANGULAR RESOLUTION

A portion of the Hα and 21 cm emission associated with feature E has been examined at 3′ angular resolution. The results imply that, while closely associated, the H^+ and H° are spatially separated into ionized and neutral regions.

The 21 cm observations were carried out with the Arecibo 305 m telescope in 1991 December, and the Hα data were obtained from CCD images of the sky taken through the 0°.8 diameter field of view of the Wisconsin large-aperture Fabry-Perot spectrometer in 1991 November. Feature E was selected for examination because it appears to have the narrowest angular structure of the Hα emission features detected on the 1° resolution maps (see Ogden & Reynolds 1985). The Arecibo map covers the rectangular region R.A. = $2^{\rm h}03^{\rm m}$ to $2^{\rm h}24^{\rm m}$ and

© American Astronomical Society • Provided by the NASA Astrophysics Data System

1995ApJ...448..715R

decl. = +37°.8 to +38°.9 (1950) and the radial velocity range −160 km s^{-1} to +100 km s^{-1} (LSR) in 0.515 km s^{-1} intervals with a velocity resolution of 0.5 km s^{-1}. This area samples the southern one-third of this feature, extending just south of the northern declination limit (+39°) of the Arecibo telescope (see Fig. 1). Figure 9 shows the 21 cm emission within a 12 km s^{-1} interval centered at −62 km s^{-1}.

An Hα image was obtained for a small region of the Arecibo map centered at 2^h10^m +38°.3, which samples an approximately 1 deg^2 area along the center line of the Hα filament as determined by Ogden & Reynolds (1985). The Hα image corresponds to the 12 km s^{-1} radial velocity interval centered at −62 km s^{-1}, the radial velocity of the Hα emission from the filament at this location. The pair of straight dashed lines indicates the approximate location and width of feature E as determined from the 1° angular resolution Hα data, while the dotted irregular "oval" denotes the extent of the high-resolution Hα image. The Hα map was obtained by taking one image with the spectrometer tuned to the filament's line center at −62 km s^{-1} and another image tuned off the line at −112 km s^{-1}. After flat-fielding the images separately, the off-line image was subtracted from the on-line image to provide an image that contained only the interstellar Hα emission associated with feature E. Several nearly coincident on-minus-off Hα images centered near 2^h10^m, +38°.3 have been combined and smoothed with a 3′ × 3′ median filter in order to reduce noise fluctuations and match the angular resolution to that of the Arecibo map. The result is displayed as a contour map superimposed on the 21 cm gray-scale map in Figure 9.

These high angular resolution images reveal that the ionized and neutral gas have quite different distributions. In the Hα image, a narrow (~0°.2) ridge of emission is found to run along the center of the Hα filament. Although the contours do not show it, fainter, more extended Hα emission fills the entire Hα field, consistent with the earlier determination that the filament's width in Hα is approximately 0°.8. The emission measure of the ridge is about 4 cm^{-6} pc, almost twice the average within the Hα field. Most of the small-scale lumpiness in the image appears to be noise at the level of 1 σ = 0.3 cm^{-6} pc, which has nearly equal contributions from photon noise and the read noise of the CCD. Incomplete subtraction of stars also contributes to a lesser extent, the worst case resulting in an apparent Hα feature ≈0°.05 in diameter at $2^h11^m30^s$, +38°.2, which makes the ridge appear to flare a little more to the southeast than it actually does.

Within the region mapped in Hα, the Arecibo 21 cm data show no associated H I down to a detection limit of 6 × 10^{18} cm^{-2}. This is confirmed by the Hat Creek observations, which provide the same limit for the 0°.6 diameter field centered at 2^h09^m +38°.4. The H I that is detected is outside the limited area of the Hα map and is also displaced from the extrapolation of the center line of the Hα filament (see Fig. 9). At 2^h14^m, +38°.0, for example, the H I is about 0°.7 south of the Hα ridge. The brightening and widening of the Hα at the eastern edge of the Hα map suggests that the H$^+$ may extend down toward the H°. Unfortunately, we were not able to obtain additional Hα images to investigate this. The available low angular resolution Hα data indicate, however, that the Hα closely follows the extrapolation of the Hα ridge toward the northeast and is not diverted significantly to the south at 2^h14^m. An examination of individual Hat Creek spectra along a 5° portion of the filament extending from 2^h38^m +40°.3 to 2^h14^m +38°.0 also indicates that the mean position of the H I has a small (≈¼°–½°) but systematic displacement to the south of the Hα. Also, there is no associated H I detected at R.A. > 2^h42^m (Fig. 2). Therefore, both the high and the low angular resolution data indicate that the neutral and ionized hydrogen associated with feature E occupy separate regions of space. This is not the first time that a systematic offset has been found in Hα and 21 cm filamentary structures. Verschuur et al. (1992) report 3°–4° separations in portions of the Orion-Eridanus "superbubble" (see also Fig. 1 in Reynolds & Ogden 1979).

Another interesting aspect of the Arecibo results is the kinematics. The width of the 21 cm line derived from the Hat Creek spectra is 23 km s^{-1} (FWHM) for feature E (see Table 1). If this were due entirely to thermal broadening, then the corresponding temperature of the H I would be 12,000 K. However, the much higher angular resolution Arecibo data indicate that most of the 21 cm line width is in fact the result of small-scale variations in the mean radial velocity. This is illustrated in Figure 10, where the spectra are compared for five 0°.2 × 0°.2 areas of the Arecibo map. Spectra a through d are at approximately ⅓ degree intervals along the H I enhancement between R.A. = 2^h14^m and 2^h17^m. Spectrum e samples the H I in the

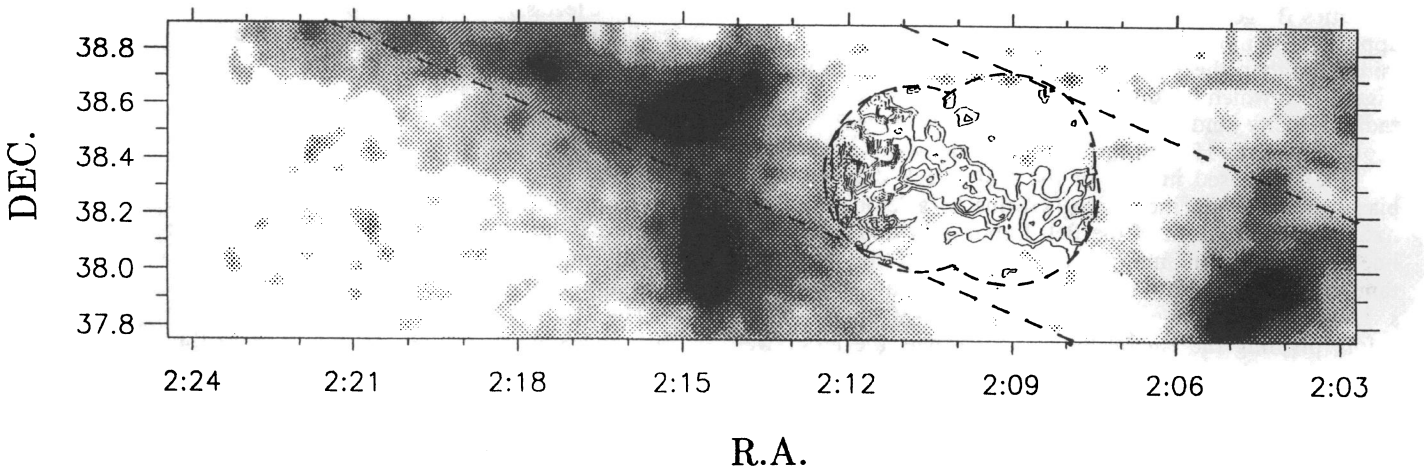

FIG. 9.—The 3′ angular resolution, −62 km s^{-1} velocity interval maps of a portion of feature E. *Gray shading:* 21 cm emission; *contours:* Hα emission. Contour values are 1.1, 1.25, 1.4, 1.55, and 1.7 R. Irregular "oval" centered at 2^h10^m +38°.3 denotes the extent of the Hα data. Straight dashed lines indicate the position and extent of the Hα filament as determined from the low angular resolution map.

© American Astronomical Society • Provided by the NASA Astrophysics Data System

1995ApJ...448..715R

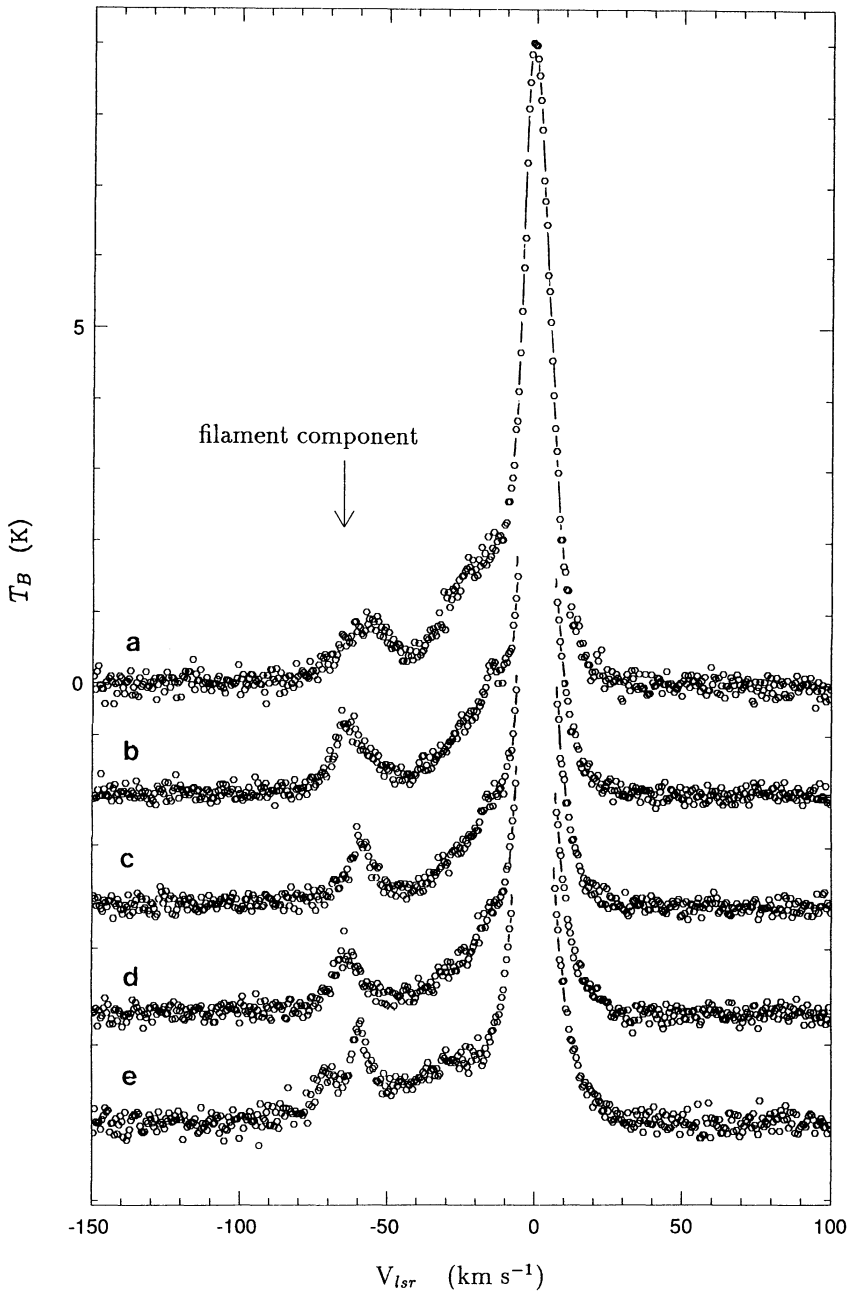

FIG. 10.—21 cm spectra for five 0°.2 × 0°.2 areas along the region of H I enhancement in Fig. 9. (*a*) $2^h17^m.4 + 38°.73$; (*b*) $2^h15^m.1 + 38°.53$; (*c*) $2^h14^m.8 + 38°.23$; (*d*) $2^h14^m.5 + 37°.88$; (*e*) $2^h05^m.2 + 37°.88$.

southwest portion of the map at 2^h05^m, +37°.88. Figure 10 shows 5–10 km s^{-1} shifts in the peak of the feature E emission component over angular distances of 20′–25′. The complex nature of the kinematics is especially obvious in spectrum e, where the line profile is split into two resolved components at −70 km s^{-1} and −60 km s^{-1}. The −60 km s^{-1} component has a line width of 5.5 km s^{-1} (FWHM), implying a gas temperature $T \leq 700$ K.

The values of $N_{\rm H\,I}$ for feature E along the 21 cm enhancement between 2^h14^m, +37°.8 and 2^h17^m, +38°.7 in Figure 9 generally vary by less than a factor of 2, ranging from about 2.4×10^{19} cm^{-2} ($2^h14^m30^s$, +37°.9; spectrum d) to 4.5×10^{19} cm^{-2} ($2^h15^m06^s$, +38°.5; spectrum b). The appearance of large intensity variations on the map along this enhancement is primarily due to the complex kinematic variations, which change the fraction of the emission component that is sampled by the 12 km s^{-1} wide radial velocity interval centered at −62 km s^{-1}. Also, the significantly lower value for $N_{\rm H\,I}$ listed in Table 1 is the result of dilution within the 0°.6 Hat Creek beam and the smoothing process used to match the higher angular resolution Hat Creek map to the Hα data map.

5. DISCUSSION

It is not clear whether these Hα-emitting H I clouds are produced by a variety of unrelated phenomena or are all the signature of some yet to be determined process that separates

© American Astronomical Society • Provided by the NASA Astrophysics Data System

1995ApJ...448..715R

them from the non–Hα-emitting clouds. In earlier Hα studies, for example, it has been suggested that enhancement A is part of a thick H I shell connected to the Per OB2 association and photoionized by the O7 III star ξ Per 13° (90 pc) to the east (Reynolds 1988), while the Hα enhancement E had been presented as a possible moderate-velocity shock propagating through a low-density ambient medium (Ogden & Reynolds 1985). No explanations have ever been proposed for the Hα enhancements C and D. It has also been suggested that enhancement B, which has no associated H I enhancement and therefore is not designated an Hα–H I cloud, may be a large, low-density H II region associated with the high $|z|$ O star HD 14633 (see Reynolds 1980).

One common factor relating these Hα–H I clouds appears to be their association with large-scale shells, loops, and filaments. This is supported by the fact that features C, F, and D also appear to be portions of one large ringlike structure, which was not detectable on the previous, less sensitive Hat Creek sky survey. This "CFD" loop is most clearly seen on the four, full-frame, full angular resolution 21 cm velocity interval maps presented in Figure 11. The ringlike morphology is clearest in the -70 km s^{-1} frame, where $N_{\rm H\,I} \approx 5 \times 10^{18}$ cm^{-2} within the 12 km s^{-1} interval. Feature E, running diagonally NE to SW through the ring, is also (coincidentally?) clearest in this frame. At lower $|v|$, the ring becomes much brighter and less circular, peaking in column density near -50 km s^{-1} (see Table 1). If this is a ring at its kinematic distance of 2800 pc, then it has a diameter of 540 pc and a total (H I + H II) mass of about $2 \times 10^5\ M_\odot$ and extends to a maximum height of 1300 pc from the Galactic midplane. It then would appear to be associated with an energetic event above the Perseus spiral arm.

Region F, where there is a gap in the Hα emission between features C and D on the -46 km s^{-1} frame in Figure 2, contains a weak emission enhancement that is clearly a part of this loop structure. The fact that the radial velocity of the enhancement in region F is -10 km s^{-1} with respect to that for C and D (see Table 1), making it more visible on the -58 km s^{-1} (21 cm) frame, is consistent with an apparent velocity gradient from eastern and western parts of the loop to this southern "gap" portion. This can be seen in Figure 2 by the "movement" of the Hα and 21 cm emission enhancements associated with the loop from the east and west sides of the map in the -34 km s^{-1} frame to the southern part in the -58 km s^{-1} frame. This is not the only emission feature showing evidence for a velocity gradient. Feature A has a maximum brightness that appears to move northward from 3^h00^m +37° in the +2 km s^{-1} frame to around 2^h35^m–2^h58^m +43° in the -10 km s^{-1} and -22 km s^{-1} frames.

The center of this 11° diameter ring is at $\simeq 2^h27^m$ +41°.4, which is only 1°.4 from the O 8.5 V star HD 14633. However, it is unlikely that there is any relationship between the two. According to models by Castor, McCray, & Weaver (1975) and Weaver et al. (1977), large shells may be produced in the interstellar medium around luminous stars by their stellar winds, but the total wind energy from an O 8.5 V star is too low to have created a structure with the size and mass of the CFD ring. The total wind energy E_w required over the lifetime of the

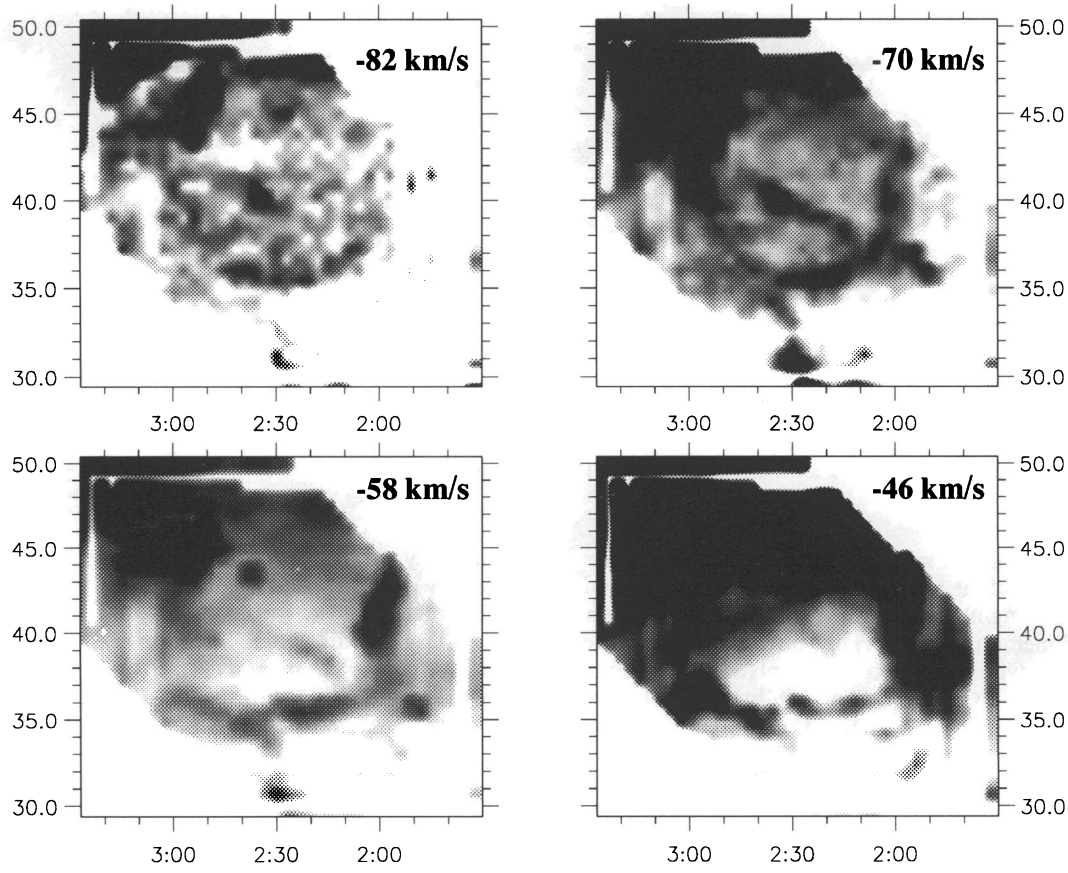

FIG. 11.—Full-frame full-resolution Hat Creek 21 cm velocity interval maps showing the H I loop (see text)

© American Astronomical Society • Provided by the NASA Astrophysics Data System

1995ApJ...448..715R

star can be expressed in these models by

$$E_w = 1.8 \times 10^{-10}\left(\frac{r_{100}}{\tau_6}\right)^2 N_{\rm swept}\ \text{ergs}\ , \qquad (2)$$

where r_{100} is the radius of the shell in units of 100 pc, τ_6 is the age of the star in 10^6 yr, and $N_{\rm swept}$ is the number of interstellar hydrogen atoms swept up into the shell. If this ring were a limb-brightened shell at the distance of HD 14633 (i.e., 2100 pc; Cruz-Gonzales et al. 1974), then $r_{100} \simeq 2.0$, and $N_{\rm swept} \gtrsim 1 \times 10^{62}$ atoms, which is the number of atoms within the ring alone, derived for a 2° wide, 11° diameter annulus having the average H I plus H II column density of C, F, and D. Therefore, to produce this ring during the $\sim 9 \times 10^6$ yr main-sequence lifetime of HD 14633, $E_w \gtrsim 9 \times 10^{50}$ ergs, which is more than 10 times larger than that available from an O 8.5 V star (Abbott 1982). Furthermore, if this ring were the limb of a shell surrounding this star, its radial velocity should correspond to that of the ambient gas. However, the ring has a velocity of -27 km s^{-1} with respect to Hα enhancement B, which is thought to be the faint H II in the low-density interstellar gas surrounding the star (Reynolds 1980). Except for its relatively low H I column density, this 21 cm ring appears similar to the multitude of other filament and loop structures of unknown origin seen in the 21 cm survey data (e.g., Heiles 1976).

A question fundamental to the nature of the Hα–H I clouds is the relationship between the ionized and the neutral hydrogen. The data suggest that the two ionization states are not well mixed. If the H° and H$^+$ were mixed, the line widths of the associated Hα and 21 cm components would be equal. However, the results presented in Table 1 clearly show that the Hα line is systematically wider. Only for cloud E are the listed widths comparable, but that is apparently only because in this cloud the 21 cm components are broadened by variations in radial velocity within the Hat Creek beam (see § 4 above). Furthermore, even though the H$^+$ and the H° are clearly associated in these clouds (Fig. 2), the pixel by pixel correlations are not strong. This is illustrated in Figure 12, where I_α is plotted against $N_{\rm HI}$ for the -52 km s^{-1} to -40 km s^{-1} velocity interval. The scatter in Figure 12 is large even though in Figure 2 this interval appears to be dominated by the large CFD loop, and there is a clear, large-scale correspondence between the Hα and 21 cm. The weakness of the correlation in Figure 12 cannot be attributed to measurement uncertainty,

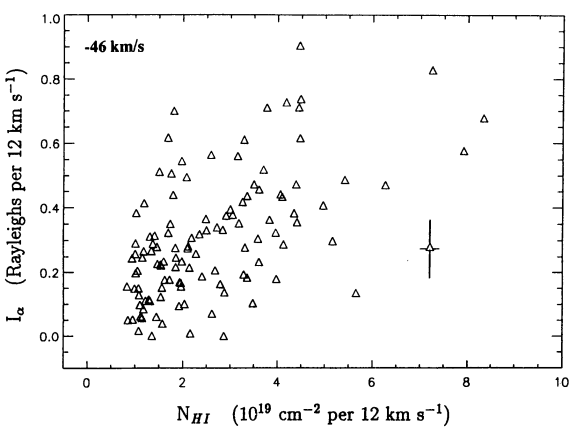

FIG. 12.—I_α vs. $N_{\rm HI}$ for the -46 km s^{-1} velocity interval map in Fig. 2. Error bars on one of the data points denote the approximate measurement uncertainties ($\pm 1\,\sigma$).

but instead is due to the fact that the correspondence between the Hα and H I breaks down on the scale of an individual pixel (1°). This can also be seen in the $+2$ km s^{-1} frames of Figure 2. In the extreme northeast corner of that frame the Hα and the H I associated with cloud A are clearly anticorrelated. These results strongly suggest that the H° and the H$^+$ occupy separate but closely related regions of space, a conclusion that also is supported by the high angular resolution observations of cloud E (§ 4).

This observed anticorrelation between the two ionization states at small angular scales is not necessarily surprising. For example, an incident Lyman continuum flux would produce clouds with separate regions of H$^+$ and H° (e.g., McKee & Ostriker 1977). If these Hα–H I clouds are in fact H I clouds bathed in an ionizing radiation field, then their Hα surface brightness provides a direct estimate of the magnitude of the incident photon flux Φ (see Field 1975). For H I clouds that are thick to the ionizing photons ($N_{\rm HI} \gtrsim 10^{18}$ cm^{-2}) but thin to the Hα ($N_{\rm HI} \lesssim 10^{21}$ cm^{-2}), as these are, the average emission measure EM $\simeq \Phi/\alpha_{\rm H}$, where $\alpha_{\rm H}$ is the effective hydrogen recombination coefficient and $\Phi = 4\pi J$ is the specific intensity integrated over solid angle. For region A the implied $\Phi = 9 \times 10^6$ cm^{-2} s^{-1}, while for C, D, and E, $\Phi = 2$–3×10^6 cm^{-2} s^{-1}. Interestingly, this latter value for the high $|z|$ clouds is equal to the interstellar ionizing flux predicted by the all-sky diffuse Hα surface brightness observed at high latitudes (Reynolds 1984; Mathis 1986; Miller & Cox 1993). Also, the resulting ratio of ionizing photon density to gas density, $n_{\rm ph}/n_e = \Phi_{\rm LC}/4n_e c \approx 1 \times 10^{-4}$, is within the range required by photoionization models of the warm ionized medium to explain the observed forbidden line intensities (Mathis 1986; Domgörgen & Mathis 1994; Sokolowski 1994). The radiation field cannot be ubiquitous, however. The upper limit on EM for cloud G is an order of magnitude below the EM of the Hα–H I clouds and implies $\Phi < 3 \times 10^5$ cm^{-2} s^{-1} in at least some regions near the Galactic midplane. Furthermore, even far above the midplane the magnitude of Φ must vary significantly on scales of 100 pc. This is implied by the fact that cloud F, located in the gap between C and D at $2^{\rm h}28^{\rm m}$, $+36°$ in the -46 km s^{-1} frames of Figure 2 and clearly part of the large loop structure discussed above, has an EM that is only one-quarter or less the EM on adjacent portions of the loop just 2°–3° away.

6. SUMMARY AND CONCLUSIONS

A comparison of velocity resolved Hα and 21 cm emission within a 10° × 12° area of the sky centered at $l = 144°$, $b = -21°$ has revealed the existence of H I clouds that have associated Hα emission. The three most prominent clouds appear to be parts of a narrow filament (E), a loop (C–D), and a thick shell (A), with emission measures EM ≈ 2 cm^{-6} pc, 3 cm^{-6} pc, and 11 cm^{-6} pc and H I column densities $N_{\rm HI} \approx 2 \times 10^{19}$ cm^{-2}, 9×10^{19} cm^{-2}, and 2×10^{20} cm^{-2}, respectively. If these clouds are at their kinematic distances, then they have ionized to neutral hydrogen column density ratios $N_{\rm HII}/N_{\rm HI} \approx 0.8$, 0.6, and 0.2, respectively, and a wide distribution away from the Galactic midplane with the filament and loop extending well outside the traditional H I disk.

The Hα–H I clouds that have been identified account for approximately 30% of the Hα and 10% of the 21 cm emission within the mapped area. The remainder appears to be associated with a more diffuse background that is apparently the superimposition of emission regions that are too faint or too

© American Astronomical Society • Provided by the NASA Astrophysics Data System

1995ApJ...448..715R

large in angular extent to be identified on the map. At high radial velocities (i.e., large distances and $|z|$ heights) the $EM/N_{H\,I}$ ratio in the background emission (Fig. 8) approaches the ratio observed for the Hα–H I clouds, suggesting that most of the H^+ and H° far from the midplane could be associated with such clouds. On the other hand, this variation with $|z|$ could be just a consequence of the fact that the H° and H^+ components of the interstellar medium have very different scale heights (Reynolds 1991). If all of the Hα were associated with Hα–H I clouds, then these clouds could account for up to about 30% of the H I. Conversely, 70% of the H I (i.e., nearly all the H I near the midplane) must have little or no associated Hα emission.

The ionization source for the Hα–H I clouds, particularly the high $|z|$ clouds, is not clear. However, both the high and the low angular resolution data suggests that the H^+ and the H° are not well mixed (§ 5). Therefore, these clouds are probably different from the partially ionized ($N_{H\,II}/N_{H\,I} \approx \frac{1}{3}$), high $|z|$ clouds proposed by Spitzer & Fitzpatrick (1993) toward HD 93521. In the Spitzer & Fitzpatrick clouds it has been argued that the H^+ and H° are mixed together in each clump of gas, requiring as yet unidentified penetrating radiation or in situ sources to produce the required ionization rate $\xi_H \approx 3 \times 10^{-15}$ s^{-1} H atom^{-1}. Since $\xi_H = \alpha_H\, EM/N_{H\,I}$, the Hα–H I clouds in Table 1, if similarly constituted, would require a $\xi_H \simeq 3$–10×10^{-14} s^{-1} H atom^{-1}, which is at least 10 times larger than the Spitzer & Fitzpatrick rate, more than 100 times that produced by cosmic rays (van Dishoeck & Black 1986), and 10 times that predicted by the decaying dark matter hypothesis (Sciama 1990). In the Hα–H I cloud E, the strongest argument against partial ionization or well-mixed H^+ and H° is provided by the apparent angular displacement between the Hα and the H I. This separation of the ionized and neutral hydrogen may be evidence for photoionization by an external radiation field (§ 5) or perhaps stratification behind a shock (Ogden & Reynolds 1985). However, it is not clear that the detailed morphology of this cloud is consistent with either of these mechanisms. Between R.A. = 2^h07^m and 2^h13^m, where the high angular resolution Hα map was made, the ridge of ionized gas does not even appear to be in contact with the neutral part of the cloud (see Fig. 9 and § 4). This seems contrary to the H^+ being a photoionized layer on an H I cloud or the H° being the region of recombination behind a hydrogen ionizing shock. Clearly, further high-resolution studies of Hα–H I clouds are needed.

These results raise a number of new questions about the interstellar medium. For example, are there generally two kinds of diffuse interstellar clouds, the traditional, non–Hα-emitting H I clouds concentrated near the Galactic midplane and the Hα–H I clouds occupying a much thicker disk? Is Hα generally associated with the loop and filamentary structures that are so prominent at high Galactic latitudes in the 21 cm surveys? Does the H I associated with Hα–H I clouds form the high-$|z|$ neutral hydrogen component ("Lockman layer") of the interstellar medium (e.g., Lockman, Hobbs, & Shull 1986)? Does the H^+ associated with these clouds form the warm ionized medium? Unfortunately, from this one $10° \times 12°$ portion (0.3% sample) of the sky, one cannot draw general conclusions about the interstellar medium. The Hα and 21 cm intensities in this region are "typical" of moderate- to high-latitude directions (§ 3.1), but any one of a number of large-scale interstellar phenomena such as superbubbles, fountains, and spiral structure could easily dominate a particular area of the sky, making generalizations invalid. Furthermore, the small number of emission features identified makes broad conclusions impossible, even if this region is representative. This situation may be remedied by more extensive, "all-sky" Hα maps, such as the one planned with the Wisconsin H-Alpha Mapper (WHAM) now under construction.

This work was supported by the National Science Foundation through grants AST 91-22701, AST 91-15703 (R. J. R. and D. T. K.), and AST 91-23362 (C. H.), the University of Wisconsin-Madison Graduate School (S. L. T.), and the National Aeronautics and Space Administration through grant HF-1049.01-93A (P. R. M.), awarded by the Space Telescope Science Institute which is operated by the Association of Universities for Research in Astronomy, Inc. for NASA under contract NAS 5-26555. We also thank the referee, John Dickey, for his insightful comments and criticisms.

REFERENCES

Abbott, D. C. 1982, ApJ, 263, 723
Bohlin, R. C., Savage B. D., & Drake, J. F. 1978, ApJ, 224, 132
Burton, W. B. B. 1971, A&A, 10, 76
Castor, J., McCray, R., & Weaver, R. 1975, ApJ, 200, L107
Cox, D. P., & Reynolds, R. J. 1987, ARA&A, 25, 303
Cruz-Gonzales, C., Recillas-Cruz, E., Costero, R., Peimbert, M., & Torres-Peimbert, S. 1974, Rev. Mexicana Astron. Af. 1, 211
Dickey, J. M., & Lockman, F. J. 1990, ARA&A, 28, 215
Domgörgen, H., & Mathis, J. S. 1994, ApJ, 428, 647
Field, G. B. 1975, in Atomic and Molecular Physics and the Interstellar Medium, Les Houches, Session XXVI, ed. R. Balian, P. Encrenaz, & J. Lequeux (Amsterdam: North-Holland/American Elsevier), 467
Heiles, C. 1976, ApJ, 208, L137
Joncas, G., Roger, R. S., & Dewdney, P. E. 1989, A&A, 219, 303
Jura, M. 1979, ApJ, 227, 798
Koo, B.-C., Heiles, C., & Reach, W. T. 1992, ApJ, 390, 108
Kutyrev, A. S., & Reynolds, R. J. 1989, ApJ, 344, L9
Lockman, F. J., Hobbs, L. M., & Shull, J. M. 1986, ApJ, 301, 380
Mathis, J. S. 1983, ApJ, 267, 119
———. 1986, ApJ, 301, 423
McKee, C. F., & Ostriker, J. P. 1977, ApJ, 218, 148
Miller, J. S. 1968, ApJ, 151, 473
Miller, W. W., III, & Cox, D. P. 1993, ApJ, 417, 579
Münch, G., & Pitz, E. 1990, in IAU Symp. 139, The Galactic and Extragalactic Background Radiation, ed. S. Bowyer and C. Leinert (Dordrecht: Kluwer), 193
Norman, C. A. 1991, in IAU Symp. 144, The Interstellar Disk-Halo Connection in Galaxies, ed. H. Bloemen (Dordrecht: Kluwer), 337
Ogden, P. M., & Reynolds, R. J. 1985, ApJ, 290, 238
Reynolds, R. J. 1980, ApJ, 236, 153
———. 1983, ApJ, 268, 698
———. 1984, ApJ, 282, 191
———. 1985, ApJ, 294, 256
———. 1988, AJ, 96, 670
———. 1991, in IAU Symp. 144, The Interstellar Disk-Halo Connection in Galaxies, ed. H. Bloemen (Dordrecht: Kluwer), 67
———. 1992, ApJ, 392, L35
———. 1993, in AIP Conf. Proc. No. 278, Back to the Galaxy, ed. S. S. Holt & F. Verter (New York: AIP), 156
Reynolds, R. J., & Ogden, P. M. 1979, ApJ, 229, 942
Sancisi, R. 1974, in IAU Symp. 60, Galactic Radio Astronomy, ed. F. J. Kerr & S. C. Simonson III (Dordrecht: Reidel), 115
Sciama, D. W. 1990, ApJ, 364, 549
Songaila, A., Bryant, W., & Cowie, L. L. 1989, ApJ, 345, L71
Sokolowski, J. 1994, preprint
Spitzer, L., Jr., & Fitzpatrick, E. L. 1993, ApJ, 409, 299
Stark, A. A., Gammie, C. F., Wilson, R. W., Bally, J., Linke, R. A., Heiles, C., & Hurwitz, M. 1992, ApJS, 79, 77
van Dishoeck, E. F., & Black, J. N. 1986, ApJS, 62, 109
Verschuur, G. L., Rickard, L. J., Verter, F., Pound, M. W., & Leisawitz, D. 1992, ApJ, 390, 514
Weaver, H., & Williams, D. R. W. 1973, A&AS, 8, 1
———. 1974, A&AS, 17, 1
Weaver, R., McCray, R., Castor, J., Shapiro, P., & Moore, R. 1977, ApJ, 218, 377

© American Astronomical Society • Provided by the NASA Astrophysics Data System